Outline of Contents

Pages

Acknowledgments

Outline of Contents I

List of Tables VII

List of Figures IX

Abstract (in Chinese) XVII

Abstract (in English) XX

Chapter 1 Electron Beam Lithography

1.1 Introduction 1

1.1.1 Historical Perspective of lithography 1

1.1.2 Solid-State Device 3

1.1.3 Lithographic Strategic 5

1.1.4 Resist Materials and Process 7

1.2 Electron Beam Lithography 8

1.2.1 Pattern Creation by an Electron Beam 8

1.2.2 Electron Scattering 12

1.2.3 Electron Beam Resists 15

1.2.4 Etch Resistance 19

1.3 Processing steps 20

1.3.1 Sensitivity and Constrast 21

1.3.2 Substrate Cleaning and Preparation 24

1.3.3 Resist Coating 25

1.3.4 Prebaking 26

1.3.5 Exposure 26

1.3.6 Postexposure Treatment 27

1.3.7 Developing 27

1.3.8 Postbaking 28

1.3.9 Etching 28

1.3.10 Stripping 29

References 30

Chapter 2 Nanoimprint Lithography

2.1 Introduction 35
2.1.1 Nanoimprint Lithography 36
2.1.2 Mold-Assisted Lithography 38
2.2 Hot-Embossing Lithography (HEL) 39
2.2.1 History of Classical Hot Embossing 39
2.2.2 Principle of Hot-Embossing Lithography 40
2.2.3 Embossed Materials 43
2.2.4 Processing Details 44
2.3 Masters, Stamps, and Molds 47
2.3.1 Master Fabrication 48
2.3.2 Polymer Masters 49
2.4 Sticking Effect 50
2.4.1 Physics of Adhesion 50
2.4.2 Surface Energy Measurement 52
2.4.3 Antisticking Layers 53
2.5 Application 58
2.5.1 Biosensor 58
2.5.2 Photodetectors and Light Emitters 59
References 61

Chapter 3 Mechanism and Modeling of Ring Pattern Formation for Electron Beam Exposure on Zwitterresist

Abstract 65
3.1 Introduction 66
3.2 Experimental 67
3.3 Results and Discussion 68
3.3.1 Sensitivity curve and formation of ring pattern 68
3.3.2 Influence of electron scattering effect and electron heating effect 68
3.3.3 Modeling the effect of electron beam dose 69
3.3.4 Throughout calculation 71
3.4 Conclusions 71
References 73

Chapter 4 Structural Transformation of Acrylic Resin Exhibits Positive and Negative Tones under Electron Beam Irradiation

Abstract 81
4.1 Introduction 82
4.2 Experimental 84
4.2.1 Materials and Sample Preparation 84
4.2.2 Sample preparation for plasma etching resistance 84
4.3 Results and Discussion 85
4.3.1 The glass transition temperature measurement 85
4.3.2 Mechanism of the chemical reaction of the zwitter-polymer upon electron beam irradiation 86
4.3.3 Sensitivity curves 88
4.3.4 Effect of baking zwitter-polymer resists for pattern resolution 89
4.3.5 Resolution of positive and negative behaviors 90
4.3.6 Etching behavior of zwitter-polymer resist 91
4.4 Conclusions 93
References 95

Chapter 5 Fabricating Micron-scale Oblique Polymer Structures by Electron Beam Writing on Resist-Coated SiO_2 Wafers

Abstract 113
5.1 Introduction 114
5.2 Experimental 116
5.3 Results and Discussion 117
5.3.1 Characterization of resist sensitivity 117
5.3.2 Etching behavior of SU-8 film 118
5.3.3 Thermal stability and reaction mechanism 119
5.3.4 Surface properties of the SU-8 film after plasma treatment 121
5.3.5 Fabrication of oblique structures 122
5.4 Conclusions 123
References 125

Chapter 6 Fabrication of Curved Structures with Electron Beam and Surface Structure Characterization

Abstract 135

6.1 Introduction 136

6.2 Experiment 138

6.3 Results and Discussion 139

6.3.1 Sensitivity curve and FTIR characterization 139

6.3.2 Thermal stability and surface microstructure after oxygen plasma treatment 140

6.3.3 Fabrication of convex and concave structures 142

6.3.4 Etching behaviors of SU-8 film 143

6.3.5 Fabrication of curved spiral structure 145

6.4 Conclusions 145

References 147

Chapter 7 Effect of Fluoroalkyl Substituents on the Reaction of Alkylchlorosilanes with Silicon Oxide Surfaces for Nanoimprint

Abstract 167

7.1 Introduction 168

7.2 Experimental 169

7.2.1 SAM Film Formation 169

7.2.2 SAM Films Analysis 171

7.2.3 Optical Ellispsometry 171

7.2.4 Surface Energy Calculations 172

7.2.5 Nanoimprint Process 173

7.3 Results and Discussions 174

7.3.1 Functional Groups of SAM 174

7.3.2 Thickness analysis 174

7.3.3 Contact Angle and Surface Free Energy 175

7.3.4 Surface Topography 177

7.3.5 Stability of FPTS and FOTS 178

7.4 Conclusions 179

References 180

Chapter 8 Fabrication of Mold with Thermosetting Polymer Patterns through Imprint Technology for Three Dimension Devices

Abstract 195

8.1 Introduction 196

8.2 Experimental 197

8.2.1 Thermosetting polymer patterns 197

8.2.2 Mold with thermosetting polymer patterns fabrication 198

8.2.3 Imprint process 199

8.2.4 Surface energy calculations 200

8.3 Results and Discussion 201

8.3.1 Phase-transition temperature measurement and surface free energy analysis 201

8.3.2 Contact angle and surface free energies 202

8.3.3 Mold with thermosetting polymer patterns and the imprinted patterns of thermoplastic polymer 203

8.3.4 Fabrication of micro-lens 205

8.4 Conclusions 206

References 208

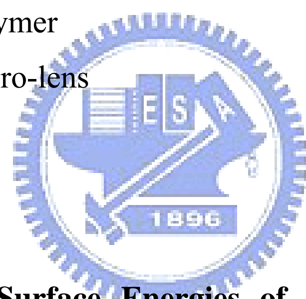

Chapter 9 Behavior and Surface Energies of Polybenzoxazines formed by Polymerization with Argon, Oxygen, and Hydrogen Plasmas

Abstract 219

9.1 Introduction 220

9.2 Experiment 221

9.2.1 Materials and Processing 221

9.2.2 Plasma treatment of BZZ films 221

9.2.3 Surface Energy 222

9.3 Results and Discussions 223

9.3.1 Reaction Mechanism Analysis 223

9.3.2 Contact Angles and Surface Free Energies 224

9.3.3 Surface Topographies 225

9.3.4 Etching Behavior 227

9.4 Conclusion 228

Reference 229

Chapter 10 Conclusions and Future Outlook 243
List of Publications 247
Introduction to Author 250

List of Tables

Pages

Table 1-1. Chemical and physical processing variables that affect lithographic performance. 22

Table 3-1.Results of scattering and heating coefficients for α_s, α_h, $\ln K_s$ and $\ln K_h$ at various dose ranges and design radiuses e 74

Table 4-1 Operating conditions for the reactive ion etcher 98

Table 4-2. Contrast ratios (γ) and threshold doses (Eth) for the zwitter-polymer resist at various thicknesses 99

Table 5-1. The fitting equation for various electron beam writing strategies 127

Table 6-1. Operating conditions for the reactive ion etcher 149

Table 6-2. Operating conditions for the electron cyclotron resonance etcher 150

Table 6-3. The fitting equations obtained from the relationship between the SU-8 film thickness and the scanning distance for the preparation of non-planar structures 151

Table 7-1 (a) Hysteresis calculated from advancing contact angless and receding angles for Water, Diiodomethane (DIM) and Ethylene Glycol (EG) on (a) FPTS and (b) FOTS monolayers as function of anneal time for monolayers formation 183

Table 7-2. Surface tension parameters calculated from the advancing contact angle for Water, Diiodomethane (DIM) and Ethylene Glycol (EG) on FPTS and FOTS monolayers with the function of anneal temperature 185

Table 7-3. Surface tension parameters and the advancing contact angle for Water, Diiodomethane (DIM) and Ethylene Glycol (EG) on FPTS monolayers for immersing in (a) HNO_3 and (b) NaOH solution with concentration of 0.1 N at 100°C as the function of immersion time 186

Table 7-4. Surface tension parameters and the advancing contact angle for Water, Diiodomethane (DIM) and Ethylene Glycol (EG) on FOTS monolayers for immersing in (a) HNO_3 and (b) NaOH solution with concentration of 0.1 N at 100°C as the function of immersion time 187

Table 8-1. Surface tension parameters calculated from the advancing contact angle for Water, Diiodomethane (DIM) and Ethylene Glycol (EG) on thermosetting polymer (SU-8) and thermoplastic polymer resists with the function of temperature 210

Table 9-1. The surface energy of dispersive component and polar component calculated from contact angle of di-iodomethane and water 231

List of Figures

Pages

Figure 1-1. Development road map for advanced lithography research and development 2
Figure 1-2. Schematic representation of a single transistor cell 4
Figure 1-3. Process sequence in the production of integrated circuit devices 4
Figure 1-4. Process sequence for producing the first two levels of an integrated circuit with a negative resists 5
Figure 1-5. Summary of the resolution capabilities of contact and projection photolithography and electron-beam and x-ray lithograph. 6
Figure 1-6. The processes of electron beam lithography 9
Figure 1-7. Uses of an electron beam to create a metallic line by the use of positive or negative resist 10
Figure 1-8. The several ways in which electron-beam lithography can be applied to create masks and patterns directly on the wafer 11
Figure 1-9. Three dimensional electron-scattering model for a resist on a thick substrate with a scanning electron beam of zero diameter 12
Figure 1-10. Monte Carlo simulated trajectories of 100 point-source electrons in a target of 1 μm thick resist on an infinitely thick silicon substrate at (a) 10-, (b) 25-, and (c) 50-keV incident energy 13
Figure 1-11. Exposure distribution at the resist-substrate interface for 1 μm-thick resist layer on a silicon substrate for 10-, 25-, and 50-keV incident energy 14
Figure 1-12. A comparison of the etch rates of thermal oxide, acrylate resist (PMMA), and AZ resist with DE-100 gas at 200 W and 0.55 torr (73.3 Pa) 15
Figure 1-13. Mechanism of radiation-induced chain scission in PMMA 16
Figure 1-14. Mechanism of radiation-induced chain scission in PMMA 17
Figure 1-15. COP, Bell Laboratories negative e-beam resists 18
Figure 1-16. Flow chart for a typical single-level resist process 21
Figure 1-17. Typical response or sensitivity curve for a negative electron-beam resist (Top) and a positive electron beam resist (Bottom) 23

Figure 2-1. Connection between applications which have led developments in lithography 36
Figure 2-2. Principle of nanoimprint lithography or hot-embossing lithography 37
Figure 2-3. (a) SEM micrograph of a SiO_2 mold with 10 nm minimum diameter pillars with a 40 nm period which are 60 nm tall, after being used 12 times. (b) SEM micrograph of a top view of 60 nm deep holes imprinted into PMMA which have a 10 nm minimum diameter and a period of 40 nm. (c) SEM micrograph of a top view of 10 nm minimum diameter metal dots with a period of 40 nm, formed by imprinting into PMMA and a lift-off process 38
Figure 2-4. Principle of mold-assisted lithography 39
Figure 2-5. Schematics of patterning by use of hot-embossing lithography. Lithography comprises steps (a)-(e), whereas steps (f) and (g) refer to the subsequent processing with the HEL mask. 41
Figure 2-6. SEM micrographs of: (a) the Si stamp with 800 nm period used to print the structure in (b); (b) printed PMMA on GaAs and (c) GaAs wires after dry etching using PMMA NIL patterning and lift off, the wire width is approximately 200 nm 42
Figure 2-7. Schematics of typical processing sequences during hot embossing used in conjunction with hydraulic systems with heating-cooling lines (top) and simple clamp devices put into an oven (bottom). 45
Figure 2-8. Schematics of processing sequences used for hot embossing of thermally modified (MAA/MA) copolymers (top) and crosslinkable polymers (bottom) 46
Figure 2-9. (a) 100 nm lines and 300 nm spacing in SiO_2. The height of the structures is 300nm. (b) AFM of a Nickel stamp made according to description as above. (c), (d) Aluminium structures on SiO_2. The thickness of the metal is 200nm 49
Figure 2-10. Contact-angle definition and principle of determination of surface energy from measurements with test liquids of different surface tension 53
Figure 2-11. Illustration of the formation of a self-assembling crosslinked siloxane layer on Si as a three-stage process as supported by physical adsorption to the OH-terminated Si covered with surface water 56
Figure 2-12. (a) Schematic top view of the DNA electrophoresis microchip. (b) SEM

displayed a portion of a nanopillar array replicated in SiO_2/Si via tri-layer NIL for PCR reactors, mixing chambers, local electrokinetic fluid pumps integrated on the same chip 59

Figure 2-13. (a) GaAs MSM photodetectors with finger spacing of 300 and 600 nm, respectively, fabricated using nanoimprint lithography. (b) SEM image of the patterned grating of PMMA/Alq_3/DCMII with a period of 200 nm by nanoimprint. (c) AFM images of the Alq_3/DCMII gratings with a period of 200 nm (left) and 300 nm (right), respectively, patterned directly by nanoimprint 60

Figure 3-1. Strategies for electron beam direct writing 67

Figure 3-2. Sensitivity curve of zwitteresist and formation of ring pattern on zwitterresist 75

Figure 3-3. Effect of electron beam dose on ring width at design r1 of (a) 1 mm to 50 mm, and (b) 100 mm to 10000 mm 76

Figure 3-4. Electron scattering effect (in solid line) and the electron heating effect (dashed line) 77

Figure 3-5. Relationship of electron heating coefficients (a) α_h and (b) $\ln K_h$ with design radius 78

Figure 3-6. Comparison of ring width obtained from experimental data and model prediction 79

Figure 3-7. (a) Effect of pattern number (pattern number of 500 means 500 lines and 500 holes) for writing time. The evaluation area is shown in the inset. The dose for positive resist is 15 $\mu C/cm^2$. The dose for negative resist is 15 $\mu C/cm^2$. (b) Dose strategy for zwitterresist is on the right hand side. E_2 is 5 $\mu C/cm^2$, and E_3 is 600 $\mu C/cm^2$ 80

Figure 4-1 DSC curve of the zwitter-polymer under electron beam irradiation with (i) 0, (ii)3, (iii)5, (iv) 7, (v) 240, (vi)280, and (vii)320 $\mu C/cm^2$ of dosage; (b) The plot of glass transition temperature with irradiated dosage by electron beam 100

Figure 4-2 Various FTIR spectra of zwitter-polymer resist films at different electron beam doses: (a) positive tone after electron beam doses of 0, 1, 3, 5, 7, 9,

15, and 30 μC/cm^2 101
Figure 4-2 (b) Negative tone after electron beam doses of (i) 240, (ii) 250, (iii) 260, (iv) 270, (v) 280, (vi) 290, (vii) 300, and (viii) 320 μC/cm^2. 102
Figure 4-2 (c) The normalized intensity of various FTIR absorption peak at 1612 cm^{-1} as a function of electron beam irradiation dosage 103
Figure 4-3 Mechanisms of the reactions occurring in the zwitter-polymer resist upon exposure to an electron beam 104
Figure 4-4 Sensitivity curves for the zwitter-polymer resist at an electron beam exposure of 40 keV for various film thicknesses. 105
Figure 4-5 The effects of soft baking and post-exposure baking (PEB) on the trench width of the positive-tone zwitter-polymer resist. 106
Figure 4-6. The effect of soft baking and post-exposure baking (PEB) on the line width of the negative-tone zwitter-polymer resist 106
Figure 4-7. The effect of dosage on pattern resolution for the positive-tone zwitter-polymer resist. (a) plot of designed trench width vs. obtained trench width; (b) plot of dosage vs. trench width 107
Figure 4-7 (c) image of dense trenches having 92-nm width; (d) image of a hole of 115-nm diameter 108
Figure 4-8. The effect of dosage on pattern resolution for the negative-tone zwitter-polymer resist: (a) plot of designed line width vs. obtained line width; (b) plot of dosage vs. line width. 109
Figure 4-8 (c) The effect of dosage on pattern resolution for the negative-tone zwitter-polymer resist: (c) image of 104-nm-wide dense lines 110
Figure 4-9. (a) Etching rate and (b) etching selectivity of the zwitter-polymer resist 111

Figure 5-1. The effect of the electron beam dose on the thickness of the resist 128
Figure 5-2. The effect of the etching gas composition on the etching rate 129
Figure 5-3. The thermal stability of various resists (oxygen plasma treatment for SU-8 resist in a PECVD chamber at 300 °C) 130
Figure 5-4. The effect of oxygen plasma treatment time on the contact angle of the SU8-50 film 131
Figure 5-5. SEM images (plan views; 105 magnification) of oxygen plasma-treated

SU8-50 resist films after treatment for (a) 5 s, (b) 20 s, (c) 40 s, and (d) 60 s 132

Figure 5-6. Oblique profiles of the SU8-50 film designed by gradient electron beam exposure 133

Figure 5-7. SEM images of the oblique profiles of the SU8-50 film that were designed with sectional distances of (a) 3 μm, (b) 5 μm, (c) 7 μm, (d) 9 μm, (e) 15 μm, and (f) 20 μm 134

Figure 6-1. Sensitivity curves for three thicknesses of the SU-8 resist at an electron-beam exposure of 40 keV 152

Figure 6-2. FTIR spectra of SU-8 films having been subjected to various doses of an electron beam. (a) The characteristic absorption near 915 cm^{-1} after exposure at 0, 2, 4, 6, 8, and 10 $\mu C/cm^2$. (b) The characteristic absorption near 1150 cm^{-1} after exposure at 0, 2, 4, 6, 8, and 10 $\mu C/cm^2$. 153

Figure 6-2 (c)FTIR spectra of SU-8 films having been subjected to various doses of an electron beam with the characteristic absorption near 3450 cm^{-1} after exposure at 0, 2, 4, 6, 8, and 10 $\mu C/cm^2$. (d) The reaction mechanism of SU-8 films after shaped electron beam exposure 154

Figure 6-3. (a) The out-gassing mass spectra at various desorption temperatures with and without oxygen plasma treatment. (b) Top-down SEM images of SU-8 film treated with oxygen plasma for 60 s. (c) Cross-sectional view of (b) 155

Figure 6-4. AFM images of the SU-8 film treated after treatment with oxygen plasma for (a) 0, and (b) 20 s 156

Figure 6-4. AFM images of the SU-8 film treated after treatment with oxygen plasma for (c) 40, and (d) 60 s 157

Figure 6-5. (a) FTIR spectra of SU-8 films having been subjected to various reaction times with oxygen plasma. (b) Effect of the oxygen plasma treatment time on the surface roughness of SU-8 film 158

Figure 6-6. Convex profiles of the SU-8 film that were designed using electron-beam writing technology. (a) Convex profile formed by various doses on the unit distance with the convex profile at unit distances of 3, 5, 7, and 10 μm. 159

Figure 6-6 Three-dimensional profiles of the SU-8 film that were designed using electron-beam writing technology. The cross-sectional SEM images of the convex profile at unit distances of (b) 3, (c) 5, (d) 7, and (e) 10 μm 160

Figure 6-7. Concave profiles of the SU-8 film that were designed using electron-beam writing technology. (a) Concave profile formed by various doses on the unit distance with the concave profile at unit distances of 3, 5, 7, and 10 μm. 161

Figure 6-7 Three-dimensional profiles of the SU-8 film that were designed using electron-beam writing technology. (a) The cross-sectional SEM images of the concave profile at unit distances of (b) 3, (c) 5, (d) 7, and (e) 10 μm 162

Figure 6-8. The etching rate and selectivity of (a) the $CHF_3/(CHF_3 + CF_4)$ gas ratio for thermal oxide and SU-8 films, and (b) the $Cl_2/(Cl_2 + O_2)$ gas ratio for poly-Si and SU-8 films 163

Figure 6-9. (a) The schematic diagram of a spiral-channel design strategy. (b) The optical microscope image of the fabricated spiral channel 164

Figure 6-9 (c) The horizontal profile of the spiral channel obtained by a surface profiler measurement. (d) The perpendicular profile of the spiral channel obtained by a surface profiler measurement 165

Figure 7-1. FTIR spectra of (a) hydrated silica at room temperature, (b) FOTS and (c) FPTS with the hydrated silica at room temperature following by annealing at 150°C for 2 hours 188

Figure 7-2. Preparation temperature dependence of film thicknesses of SAMs for (a) FPTS and (b) FOTS on silicon oxide substrates 188

Figure 7-3. Surface energy of FPTS and FOTS monolayers calculated from the contact angles of di-iodomethane, glycol and water as a function of immersion time for monolayers formation 189

Figure 7-4. Surface energy of FPTS and FOTS monolayers calculated from the contact angles of di-iodomethane, glycol and water as a function of anneal temperature for condensation of self-assembled reaction 189

Figure 7-5. AFM images (1 μm ×1 μm) of SAMs for the (a) FPTS and (b) FOTS surface for immersion time of 30 minutes at anneal time of 150°C 190

Figure 7-6. AFM images (1 μm ×1 μm) of the resist surface after separated from the mold with the (a) silicon oxide film, (b) FPTS and (c) FOTS SAMs 191

Figure 7-7 SEM images of the iso-trench fabricated by using the mold with the (a) silicon oxide film, (b) FPTS and (c) FOTS SAMs in nanoimprint lithography. The feature sizes of the iso-trench are 120 nm (right) and 60 nm (left), respectively 192

Figure 7-8. The contact angle of water of SAMs for (a) FPTS and (b) FOTS surface treated with oxygen plasma with a series of time 193

Figure 8-1. DSC curve of the chemical-amplified resist. (a) thermosetting polymer (SU-8), and (b) thermoplastic polymer resists (22A4) 212

Figure 8-2. Polt of stress versus temperature for thermoplastic polymer resist (22A4) 212

Figure 8-3. Surface energy versus temperature of (a) thermoplastic polymer resist (22A4), and (b) thermosetting polymer (SU-8). Surface energies were calculated from the contact angles of di-iodomethane, glycol and water as a function of anneal temperature 213

Figure 8-4. The SEM top-view images of the surface mold with thermosetting pattern (SU-8) for (a) iso-lines, and (b) dense cylinders. The thermoplastic polymer resist (22A4) with 650 nm of thickness imprinted by mold with thermosetting pattern (SU-8) for (c) iso-trenches and (d) dense contact holes 214

Figure 8-5. The shrink factor as a function of the feature size of thermosetting polymer pattern on mold for (a) iso-trenches, and (b) dense contact holes 215

Figure 8-6. (a) The exposure strategy of electron beam for fabricating microlens of thermosetting polymer. (b) The SEM images of 45°-tilt angle of the thermosetting polymer microlens for mold before imprint as the unit distance is (b) 3 μm, (c) 5 μm, and (d) 7 μm 216

Figure 8-7. The thermoplastic polymer resists (22A4) with 3.3 μm of thickness imprinted by thermosetting microlen mold. SEM images of 40°-tilt angle as thermoplastic polymer resists imprint the thermosetting microlens with (a) 3 μm, (c) 5 μm, and (d) 7 μm of unit distance 217

Figure 8-8. (a) SEM top-view image, and (b) SEM image of 0°-tilt angle for PDMS microlens fabricated by the reversal mold of thermoplastic polymer resists as unit distance is 3 μm 218

Figure 9-1. (a) FTIR spectra of (i) BZZ film and PBZZ films treated by (ii) argon, (iii) oxygen, and (iv) hydrogen plasma for 90 sec. The characteristic absorption near 948, 1031, 1232, 1329, and 1496 cm^{-1} 232

Figure 9-1. (b) FTIR spectra of (i) BZZ film and PBZZ films treated by (ii) hydrogen, (iii) argon, and (iv) oxygen plasma for 90 sec. The characteristic absorption between 2500 and 3600 cm^{-1} 233

Figure 9-2. Contact angle of (a) di-iodomethane and (b) water of argon, oxygen, and hydrogen plasma treated BZZ film with the increase of plasma treatment time 234

Figure 9-3. Surface free energies of argon, oxygen, and hydrogen plasma treated BZZ film with the increase of plasma treated time 235

Figure 9-4. (a) Scanning electron micrographs of PBZZ film that were treated with argon plasma for the series time 236

Figure 9-4. (b) Scanning electron micrographs of PBZZ film that were treated with oxygen plasma for the series time 237

Figure 9-4. (c) Scanning electron micrographs of PBZZ film that were treated hydrogen plasma for the series time 238

Figure 9-5. (a)AFM images (1 μm ×1 μm) of the PBZZ surface modified with argon plasma for the series reaction time 239

Figure 9-5. (b) AFM images (1 μm ×1 μm) of the PBZZ surface modified with oxygen plasma for the series reaction time 240

Figure 9-5. (c) AFM images (1 μm ×1 μm) of the PBZZ surface modified with hydrogen plasma for the series reaction time 241

Figure 9-6. Effect of the argon, oxygen, and hydrogen plasma-polymerization with increase of plasma treated time on the rms roughness of the PBZZ film at of 1 μm ×1 μm image size 242

Figure 9-7. The etching rate of the PBZZ films as the argon, oxygen, and plasma treated for 90 sec in CF_4 plasma 242

摘　要

非主流微影技術（alternative techniques）在近二十年蓬勃發展，目的在取代光學微影技術，高價格機台與光波長極限讓光學微影發展受限制。而能夠取代光學微影最具代表性的技術是電子束與奈米壓印微影技術，電子束微影最主要的特質如下所示：

1. 具備非常高解析度圖案製造能力，甚至可達原子等級。
2. 非常彈性的技術，適用於各種材料。

然而，電子束微影在產速上受到限制，造成電子束產品高單價，目前在微影主流競爭上，仍未完全取代光學微影，而奈米壓印微影是近年來新興的技術，具備高產速製造奈米元件的特性，其中熱壓印微影在圖案解析度上，沒有光學微影繞射或是電子束散射以及其他微影技術的問題，因此而受到矚目。

在本論文中，我們焦點將放在高分子材料於電子束與奈米壓印技術兩部分研究上：

（1）高分子在電子束照射下的行為與應用

線性壓克力高分子（PMMA）受到電子束照射下會產生結構上的轉變，而成為交聯壓克力高分子被定義為雙性高分子，並在敏感度曲線顯現出來。因此，這類高分子可在同一層薄膜上同時展現出正與負型光阻特性並產生環形圖案，此現象可歸類為電子束的散射與熱效應所造成，而使得環形圖案半徑與電子束劑量的關係圖顯示出兩個區域，交界劑量定義在 600 $\mu C/cm^2$，對此現象我們建立電子束的散射與熱效應的半實驗數學行為模式，結果顯示在低劑量時，電子束散射效應控制了解析度，而在高劑量時，熱效應控制了解析度。而化學結構的變化上，壓克力高分子受電子束低劑量照射時（$< 30\ \mu C/cm^2$），會產生雙鍵，而在電子束高劑量照射下（$> 240\ \mu C/cm^2$），則雙鍵會產生聚合反應，並產生交聯結構。如此藉由電子束來控制壓克力高分子線性與交聯結構，非常適合應用在半導體領域中的正與負型光阻，並能夠在同一圖層上製造出正與負型光阻，非常有利於半

導體圖案設計。不論正、負型光阻，其對比度與臨界劑量皆隨著厚度增加，對比度仍然以正型光阻較為優良。

環氧樹脂材料（SU-8）也能夠利用電子束技術來製造斜面與曲面結構，我們先對 SU-8, PMMA, 與 KrF 三種光阻研究其對比度、敏感度、蝕刻與熱性質，並找出適合製造三維結構的高分子。在這些光阻中，環氧高分子（SU-8）顯示出最低對比度與最佳熱穩定度，所以被認定為可製造立體圖案的最佳高分子。我們所製造三維結構的方法是將環氧樹脂薄膜分成五個區域曝光，分別施加不同劑量，以做成斜面結構。並討論氧電漿處理後表面結構、反應機構與疏水性質，結果顯示表面經過電漿處理會增加表面粗糙度，而減少表面釋氣現象增加環氧樹脂膜的穩定度。並評估電子束劑量與環氧樹脂斜面角度的關係，利用曝光區域的擴大來控制斜面角度，結果顯示當曝光單位距離為 10 μm，可達到較平坦的表面結構。由同樣的方式可製造出凹面與凸面結構，並可製造出具實用價值的螺旋結構，此可應用在微流體晶片上，會有曲面結構的產生主要是因為電子束散射的原因，電子束散射模糊了階梯狀結構，讓曲面更加光滑。然而，隨著曝光單位距離加大時，階梯狀結構則會慢慢出現，而所有的曲面皆是藉由電子顯微鏡來分析曲面結構。同樣的利用單位曝光距離改變，可製造出不同曲率半徑的凹面與凸面結構，而這種結構可用於控制流體在晶片上流動的速度，以減少微流體晶片上微幫浦的使用個數。另外，螺旋結構可縮小設計為流體晶片的體積，我們討論了螺旋結構的製造方式，並製造出螺旋結構的原始模型。

（2）在二氧化矽表面合成自組裝單層膜的研究及其在奈米壓印微影上的應用

在奈米壓印（nanoimprinting）技術中，母模（mold）與高分子在高溫高壓之下接觸，高分子因為超過玻璃轉移溫度而流動，形成與母模上圖案互補的圖形，在此種情況下，高分子與母模之間的作用力成為一個重要的議題，而母模與高分子之間的作用力強度可藉由表面張力計算來分析。一般而言，母模表面張力愈小，黏著力愈小，母模與高分子愈容易分離。在本實驗中，3,3,3-三氟丙烷基三氯矽烷[trichloro(3,3,3-trifluoropropyl)silane, FPTS] 與 1H, 1H, 2H, 2H-全氟辛烷基三氯矽烷[trichloro(perfluorooctyl)silane, FOTS] 被用作在二氧化矽表面形成自

組裝膜（self-assembled layer），來當成防止黏著層，使母模脫離高分子時，降低界面的黏著力。自組裝薄層表面官能基可藉由紅外線光譜儀來進行分析。而自組裝單層膜的品質則取決於晶片表面二氧化矽與反應物的浸泡時間與加熱去水縮合反應溫度，這些特性可藉由橢圓測厚儀與溶劑接觸角的測量分析，並可計算自組裝單層膜的表面自由能。結果顯示在母模上生成 FPTS 或是 FOTS 的自組裝單層膜可減少在奈米壓印過程中所產生的缺陷，並在壓印過程中能夠降低高分子膜表面的粗糙度。在母模上生成 FOTS 的自組裝單層膜可將其表面自由能降低約至 8 mJ/m^2，在壓印過程中消除了所有在高分子表面的缺陷，讓表面更加光滑，甚至提升了圖案解析度，而使得圖案解析度到達 60 nm。由此可證實表面能是影響奈米壓印圖案品質的重要因素。

母模一般是經由微影技術定圖案並通過漫長半導體製成而成，過程十分繁瑣，使得母模的價格居高不下，利用熱固型高分子作為圖案並當成是母模的一部份，在超過熱塑性高分子的玻璃轉移溫度時，仍可保持圖案形狀，這樣的方法使得母模的製造流程不需經過蝕刻與去光阻製程，而大幅降低母模製造成本。使用熱固性高分子作為圖案模型進行熱壓的技術主要基於兩種可能性：(1) 在矽晶片上製造熱固性圖案在半導體製程上是非常純熟的技術；(2) 熱固型高分子因為其網狀交聯的結構，所以沒有明顯的玻璃轉移溫度，且其軟化溫度比熱塑性高分子高出甚多。在本實驗中，環氧樹脂類高分子被用來當作熱固性圖案結構，並熱壓熱塑性高分子，利用電子束製造出來的山丘狀圖案結構增加了環氧樹脂與矽晶片之間的接觸面積，進而增加環氧樹脂與矽晶片之間的附著力。奈米壓印技術製造出來的圖案將由電子顯微鏡來分析。由於高分子與高分子接觸時會有較大的黏著力，在分離製程時，會驅動熱塑性高分子產生收縮的情況，會使得圖案縮小，我們定義此為收縮因子（shrinkage factor），發現收縮因子與圖案大小有直接關係，此因兩高分子分離時，表面吸附力驅動熱塑性高分子填補分離時的位置所造成。另外，可利用熱塑性高分子上面的微透鏡圖案來翻印聚雙甲基矽烷（polydimenthyl siloxane，PDMS）的微透鏡。

Abstract

Alternative techniques to cost-intensive or limited-access fabrication methods with nanometre resolution have been under development for nearly two decades. Two clear examples are electron beam and nanoimprint lithography technologies. The main attributes of the electron beam lithography are as following:

1. It is capable of very high resolution, almost to atomic level.
2. It is a flexible technique that can work with a variety of materials and almost infinite number of patterns.

Nevertheless, electron beam lithography is a technique with limited throughput, leading to high costs in device production. The contest of lithography techniques for reliable fabrication of future integrated nanometer-scaled devices is not yet settled. Nanoimprint is an emerging lithographic technology that promises high-throughput patterning of nanostructures. Based on the mechanical embossing principle, nanoimprint technique can achieve pattern resolutions beyond the limitations set by the light diffractions or beam scatterings in other conventional technique.

In this thesis, we focus on the subjects which based on the materials for electron beam and nanoimprint lithography:

(1)The behaviors of polymer under electron beam irradiation and the applications

Structural transformation of polymers from linear to crosslinked structure by using electron beam irradiation has been defined as the zwitter-polymers. The novel sensitivity curve has been determined for the zwitter-polymer. The irradiation dose in the center can create a ring pattern due to simultaneous exhibition of the positive tone

and negative tone of zwitter-polymer. The natural logarithm dependence of ring width and electron beam dose is linear in two ranges, irrespective of the dot design radius. The heating effect is identified from 600 $\mu C/cm^2$. Mathematical modeling for the prediction of ring width for zwitter-polymer is achieved by considering the electron scattering and heating effects. The results of experimental measurement and modeling on ring width show a very good correlation. Furthermore, the polymer may exhibit either linear and crosslinked behavior depending on dosage of the electron beam irradiation. The property change from the structural transformation is suitable for application of positive and negative tone resists in semiconductor field. The contrast ratio and threshold dose both increase with increasing resist thickness for both the positive and negative tones, however, the positive tone exhibits better contrast than the negative tone.

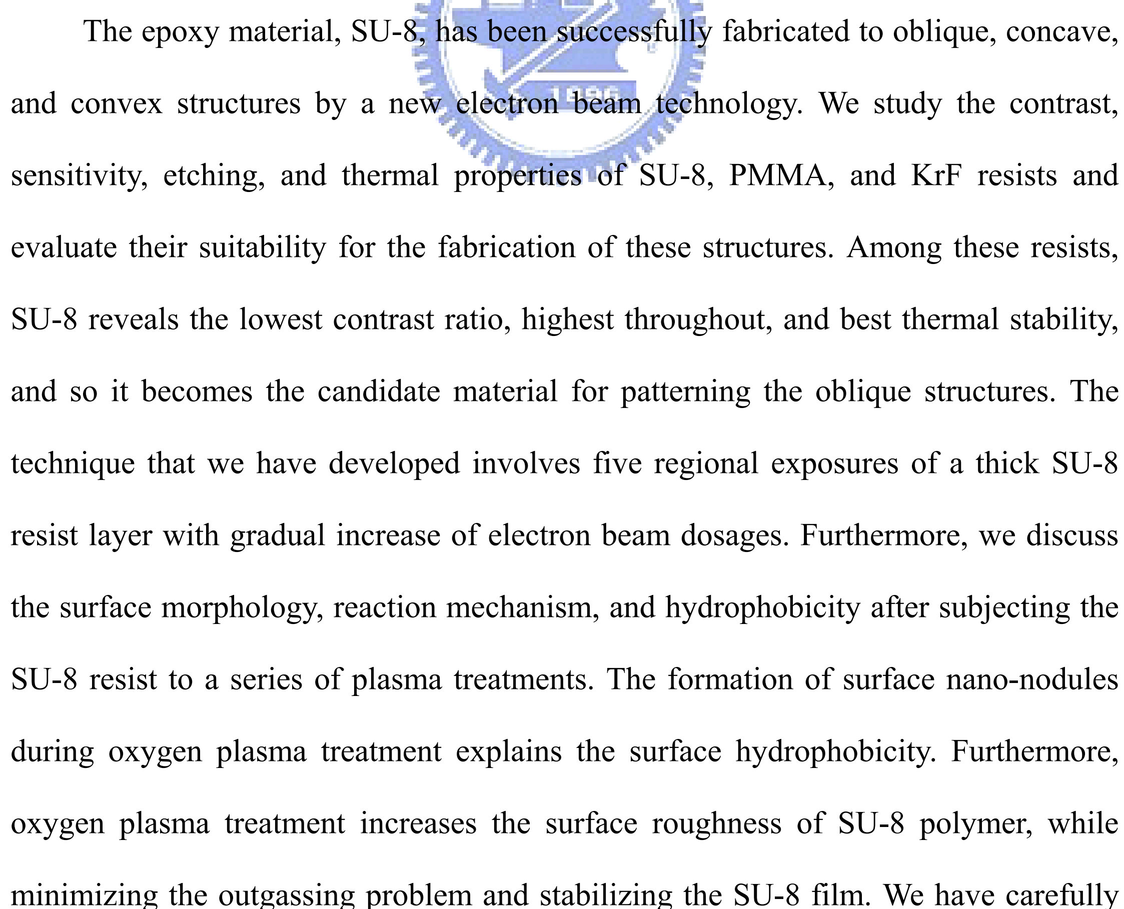

The epoxy material, SU-8, has been successfully fabricated to oblique, concave, and convex structures by a new electron beam technology. We study the contrast, sensitivity, etching, and thermal properties of SU-8, PMMA, and KrF resists and evaluate their suitability for the fabrication of these structures. Among these resists, SU-8 reveals the lowest contrast ratio, highest throughout, and best thermal stability, and so it becomes the candidate material for patterning the oblique structures. The technique that we have developed involves five regional exposures of a thick SU-8 resist layer with gradual increase of electron beam dosages. Furthermore, we discuss the surface morphology, reaction mechanism, and hydrophobicity after subjecting the SU-8 resist to a series of plasma treatments. The formation of surface nano-nodules during oxygen plasma treatment explains the surface hydrophobicity. Furthermore, oxygen plasma treatment increases the surface roughness of SU-8 polymer, while minimizing the outgassing problem and stabilizing the SU-8 film. We have carefully

evaluated the effects of the electron beam writing dose and the design of the exposure area with respect to the inclined angle of the fabricated structure.

Convex, concave, and spiral structures are fabricated successfully by using a gradient dosing strategy. The interface between two shot sections is smoothed by the electron scattering effect. The curved profile is fabricated at various curvatures, and characterized using scanning electron microscopy and a profiler. In addition, a spiral structure is fabricated that possesses the advantageous feature of having a small chip area. We discuss a method of characterizing the spiral structure.

(2) **The studies of self-assembled monolayer on the silicon oxide surface and fabrication of microlens**

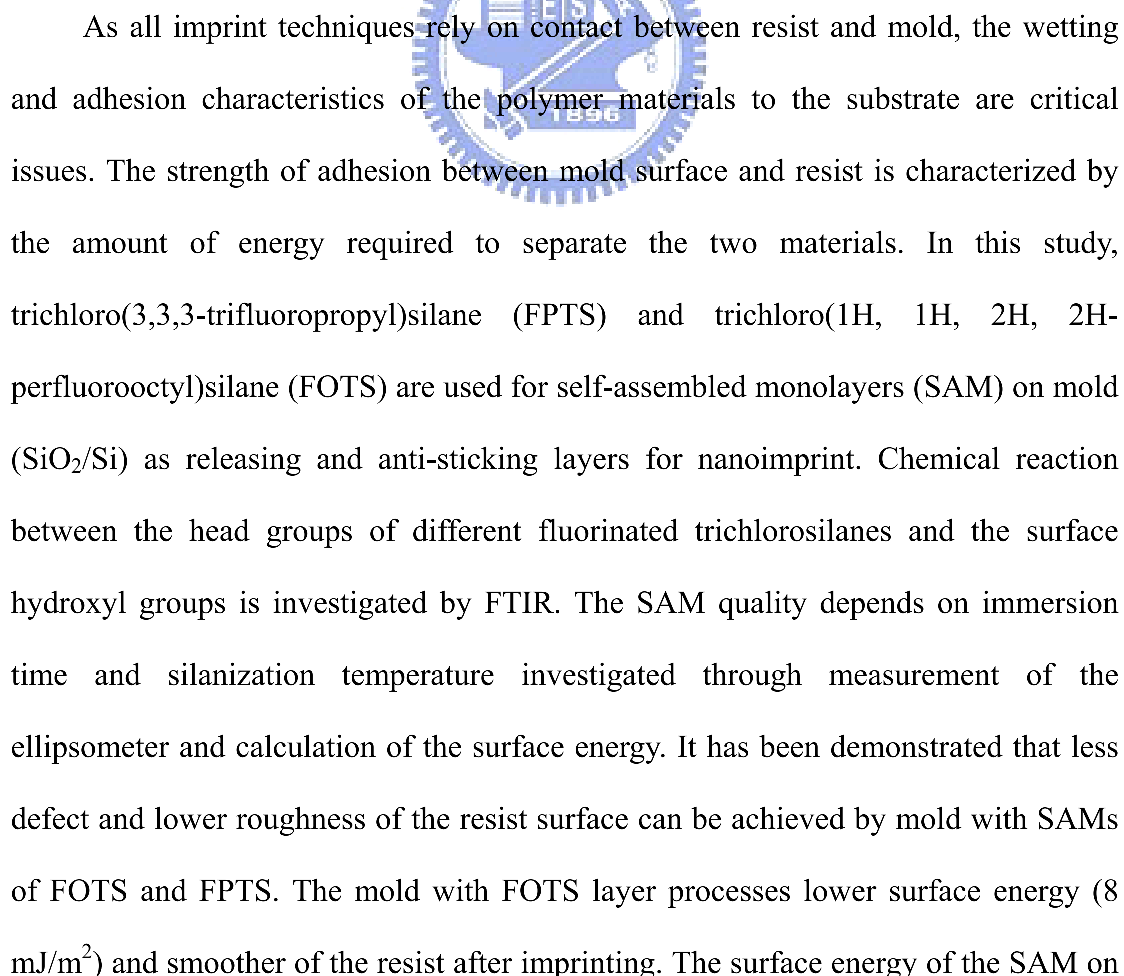

As all imprint techniques rely on contact between resist and mold, the wetting and adhesion characteristics of the polymer materials to the substrate are critical issues. The strength of adhesion between mold surface and resist is characterized by the amount of energy required to separate the two materials. In this study, trichloro(3,3,3-trifluoropropyl)silane (FPTS) and trichloro(1H, 1H, 2H, 2H-perfluorooctyl)silane (FOTS) are used for self-assembled monolayers (SAM) on mold (SiO_2/Si) as releasing and anti-sticking layers for nanoimprint. Chemical reaction between the head groups of different fluorinated trichlorosilanes and the surface hydroxyl groups is investigated by FTIR. The SAM quality depends on immersion time and silanization temperature investigated through measurement of the ellipsometer and calculation of the surface energy. It has been demonstrated that less defect and lower roughness of the resist surface can be achieved by mold with SAMs of FOTS and FPTS. The mold with FOTS layer processes lower surface energy (8 mJ/m^2) and smoother of the resist after imprinting. The surface energy of the SAM on

mold (SiO_2/Si) dictates the results in quality of better resist surface and the pattern formation.

Mold fabrication for imprinting can be significantly simplified by using specialized crosslinking polymers for pattern definition on silicon wafer. The thermosetting polymer pattern can be used on silicon molds for imprint technology because of two possibilities: (1) the silicon oxide molds with thermosetting polymer pattern can be obtained by any conventional semiconductor technology; (2) thermosetting polymers have no obvious T_g because of cross-linking structure, whereas decreases the hardness as the temperature increasing over their T_g. In this work, the SU-8 resist is used as the thermosetting polymer pattern on silicon wafer for molds. Thermal properties of the thermosetting and thermoplastic polymers are tested for imprinting pattern and imprinted resist. The hill-like structure fabricated by electron beam strategy for thick film is used to increase the adhesion between pattern and silicon wafer. The resolution of the thermoplastic polymer resist pattern imprinted by thermosetting polymer pattern is investigated by SEM. The shrink factor of the feature size after separation between thermosetting polymer pattern and thermoplastic polymer resist is utilized to define the feature size after imprinting. In addition, a microlens of polydimenthyl siloxane (PDMS) has been fabricated by replication using the thermoplastic polymer resist after imprinting by the mold with microlens structure of the thermosetting polymer (SU-8).